Summer Students Internship

Final Report

Search for high transverse momentum $H \to b\bar{b}$ with CMS

Eleonora Pasino

Supervisor: Caterina Vernieri

September 27, 2017

Contents

Introduction

In the Standard Model, the Higgs mechanism is responsible for electroweak symmetry breaking and the mass of all elementary particles [2]. Although the Higgs boson has been discovered [11, 12], its observed properties and couplings are only measured with a precision at the level of 10% or worse [13]. In particular, the LHC Run 1 data was not sufficient to establish the coupling of the Higgs boson to bottom quarks: despite the dominant branching ratio of the Higgs boson to a bottom quark-antiquark pair $b\bar{b}$ 58% [15], this type of decay has not been observed yet.

The traditional strategy to search for $H \to b\bar{b}$ decays at a hadron collider is to use events in which the Higgs boson is produced in association with a W or Z boson decaying leptonically, in order to suppress the large background from the QCD production of b quarks (VH production mode).

Recent theoretical and experimental developments [15] propose to use the gluon fusion production mode (ggF) with the requirement of a high-p_t Higgs boson in association with a high-p_t jet. [2]. The search for $H \to b\bar{b}$ in the ggF production mode was considered impossible because of the irriducible QCD background coming from b quarks production, which is order of magnitude larger than the Higgs production cross section, as shown in Fig.0.1. [16].

The focus of my work during the Summer Students Internship at Fermilab was on the gluon fusion production mode. The main target was to contribute to the optimization of the event selection by analyzing the discrimination between the gluon fusion and vector boson fusion processes.

In this report, the results of the search for standard model Higgs boson with $H \to b\bar{b}$ decays are reported using simulated signal events of pp collisions at $\sqrt{s} =$ 13 TeV in the CMS detector at LHC.

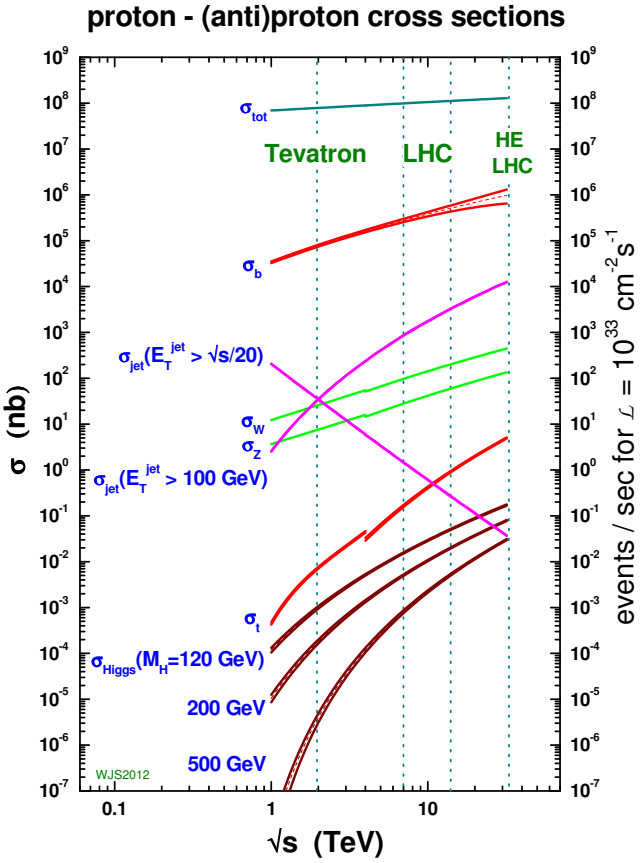

Figure 0.1: Scheme of the proton-proton cross sections [16]

Chapter 1

Higgs Boson

1.1 General properties

The Higgs boson is an elementary particle in the Standard Model (SM) of particle physics. It is the quantum excitation of the Higgs field, a fundamental field of crucial importance to particle physics theory [30]. The question of the existence of the Higgs field became the last unverified part of the SM of particle physics, and for several decades, was considered the central problem in particle physics.

On 4 July 2012, the discovery of a new particle with a mass between 125 and 127 GeV/c^2 was announced by CMS and ATLAS from indipendent observations [5]: the measurements performed by ATLAS and CMS have been mainly based on the study of the decay channels $H \to \gamma\gamma$ and $H \to ZZ \to 4l$ where $l = e$ or μ [5]. The particle has been found to behave, interact, and decay as predicted by the SM, as well as having even parity and zero spin, two fundamental attributes of a Higgs boson. More studies are needed to verify with higher precision that the discovered particle has properties matching those predicted for the Higgs boson by the SM, or whether, as predicted by some theories, multiple Higgs bosons exist. The precision achieved by LHC during Run I and II on the couplings is between 10% and 20% [32, 33].

1.2 Mechanisms of production

The SM predicts that Higgs bosons could be produced in a number of ways, although the probability of producing a Higgs boson in any collision is always expected to be very small (only 1 Higgs boson per 10 billion collisions at LHC).

The most common expected processes for Higgs boson production are the following [5]:

- Gluon-gluon fusion (ggF): Fig.1.1*a*. Cross section: 43.92 pb. [34]

  If the collided particles are hadrons such as the proton then it is most likely that two of the gluons binding the hadron together collide. The easiest way to produce a Higgs particle is if the two gluons combine to form a loop of virtual quarks. Since the coupling of particles to the Higgs boson is proportional to their mass, this process is more likely for heavy particles. In practice it is enough to consider the contributions of virtual top and bottom quarks (the heaviest quarks). This process is the dominant contribution at the LHC and it is the most abundant channel.

- Vector boson fusion (VBF): Fig.1.1*b*. Cross section: 3.748 pb. [34]

  Another possibility when two fermions collide is that the two exchange a virtual W or Z boson, which emits a Higgs boson. The colliding fermions do not need to be the same type. This process is the second most important for the production of Higgs particle. It has a very distinctive topology because in addition to the Higgs boson, we expect to have two quarks with large pseudorapidity.

- Higgs Strahlung (VH): Fig.1.1*c*. Cross section: 1.380 pb. [34]

  If an elementary fermion collides with an anti-fermion the two can merge to form a virtual W or Z boson which, if it carries sufficient energy, then it can emit a Higgs boson. This process is only the third largest, because the LHC collides protons with protons, making a quark-antiquark collision.

- Top fusion (ttH): Fig.1.1*d*. Cross section: 0.5085 pb. [34]

  The final process that is commonly considered is by far the least likely. This process involves two colliding gluons, which each decay into a heavy quark–antiquark pair. A quark and antiquark from each pair can then combine to form a Higgs particle.

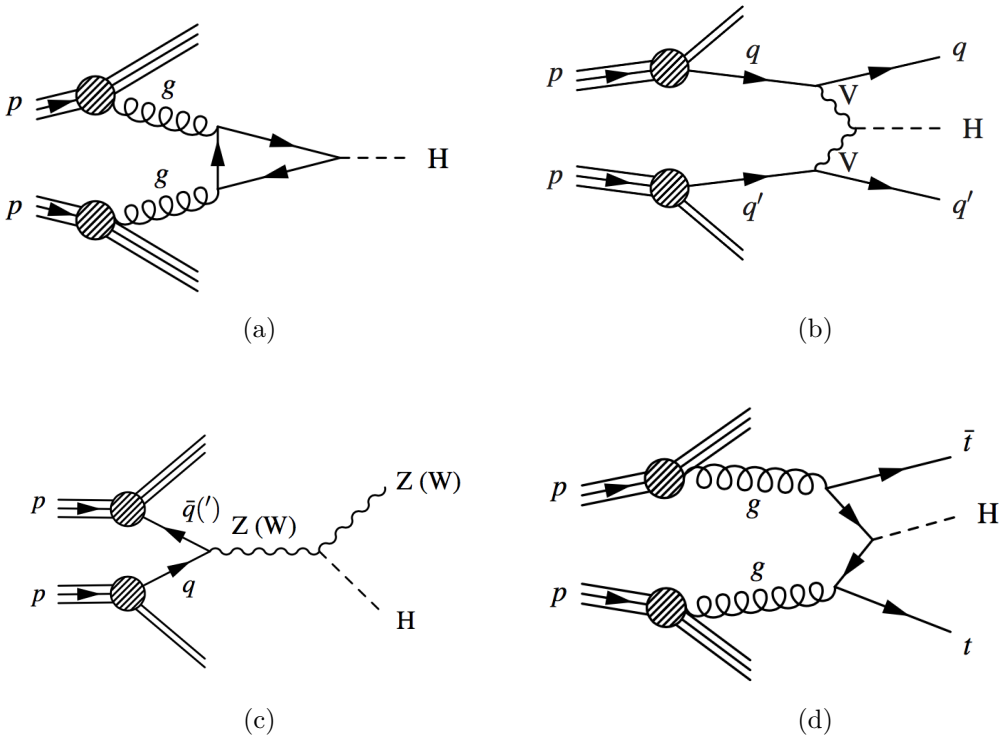

Figure 1.1: ***Mechanisms of Higgs production***
(a): Gluon-gluon Fusion
(b): Vector Boson Fusion
(c): Higgs Strahlung
(d): Top Fusion

1.3 Decay channels

Quantum mechanics predicts that if it is possible for a particle to decay into a set of lighter particles, then it will eventually do so. This is also true for the Higgs boson. The likelihood with which this happens depends on a variety of factors including the difference in mass and the strength of the interactions. Most of these factors are fixed by the SM, except for the mass of the Higgs boson itself. For a Higgs boson with a mass of 125 GeV/c^2 the SM predicts a mean life time of about 1.6×10^{-22} s.

Since it interacts with all the massive elementary particles of the SM, the Higgs boson has many different processes through which it can decay, see Fig.1.2 [5]. Each of these possible processes has its own probability, expressed as the branching ratio, the fraction of the total number decays that follows that process. The SM predicts these branching ratios as a function of the Higgs mass.

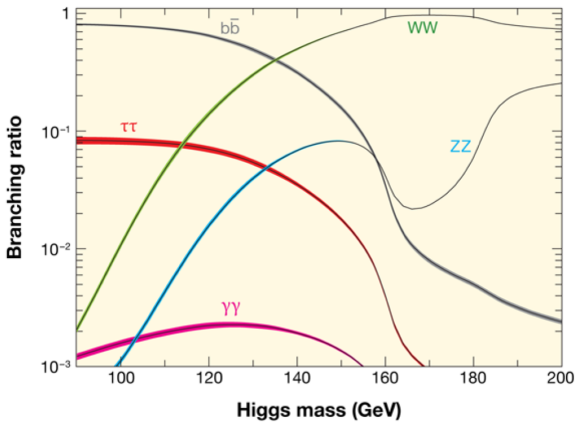

H decay channel	Branching ratio	Mass resolution (%)
$H \to \gamma\gamma$	2.28×10^{-3}	1-2
$H \to ZZ\ (\to 4l)$	2.64×10^{-2}	(1-2)
$H \to WW\ (\to l\nu l\nu)$	2.15×10^{-1}	(20)
$H \to \tau\tau$	6.32×10^{-2}	15
$H \to bb$	5.77×10^{-1}	10

Figure 1.2: The Standard Model prediction for the branching ratios of the different decay modes of the Higgs particle [5].

One way that the Higgs can decay is by splitting into a fermion–antifermion pair. As general rule, the Higgs is more likely to decay into heavy fermions than light fermions. For a Higgs mass of 125 GeV/c^2 the SM predicts that the most common decay is into a bottom–antibottom quark pair, which happens 57.7% of the time. The second most common fermion decay at that mass is a tau–antitau pair, which happens only about 6.3% of the time. Another possibility is for the Higgs to split into a pair of massive gauge bosons. The most likely possibility is

for the Higgs to decay into a pair of W bosons, which happens about 21.5% of the time for a Higgs boson with a mass of 125 GeV/c^2. The W bosons can subsequently decay either into a quark and an antiquark or into a charged lepton and a neutrino. A cleaner signal is given by decay into a pair of Z-bosons (which happens about 2.6% of the time), if each of the bosons subsequently decays into a pair of charged leptons (electrons or muons).

As seen in the table of Fig.1.2, the channels $H \to \gamma\gamma$ and $H \to ZZ \to 4l$ have no large cross sections but they are preferred as "golden" channels thanks to high mass resolutions (1-2%) and clean signals. The other three channels are not excluded from use but there are several difficulties. Compared with other channels, the channel $H \to WW \to l\nu l\nu$ has a large branching ratio but the Higgs mass resolution is very low (20%) because of neutrinos produced in the final states. The channels $H \to \tau\tau$ and $H \to bb$ have no clean signals because of a low mass resolution (15% and 10%, resp.) and large backgrounds [5].

The most important difference between the decay channels is that while the first four decays of the table in Fig.1.2 have already been measured at LHC, $H \to b\bar{b}$ has not been observed yet. For this reason, the focus of this search is on the $H \to b\bar{b}$ decay mode.

Chapter 2

CMS Experiment

2.1 Large Hadron Collider

The Large Hadron Collider (LHC) is the biggest and most powerful particle accelerator of the world, located at CERN near Geneva [17]. It lies in a tunnel 27 kilometres in circumference, as deep as 175 metres beneath the France–Switzerland border.

Figure 2.1: Scheme of the LHC ring

The collider tunnel contains two adjacent parallel beamlines (or beam pipes) each containing a beam, which travel in opposite directions around the ring. The beams intersect at four points around the ring, which is where the particle collisions take place. Before being injected into the main accelerator, the particles are prepared by a series of systems that successively increase their energy. The first

system is the linear particle accelerator LINAC 2 generating 50 MeV protons, which feeds the Proton Synchrotron Booster (PSB). There the protons are accelerated to 1.4 GeV and injected into the Proton Synchrotron (PS), where they are accelerated to 26 GeV. Finally the Super Proton Synchrotron (SPS) is used to further increase their energy to 450 GeV before they are at last injected into the main ring [5, 18]. A general scheme of the LHC ring and detectors is shown in Fig.2.2 [5].

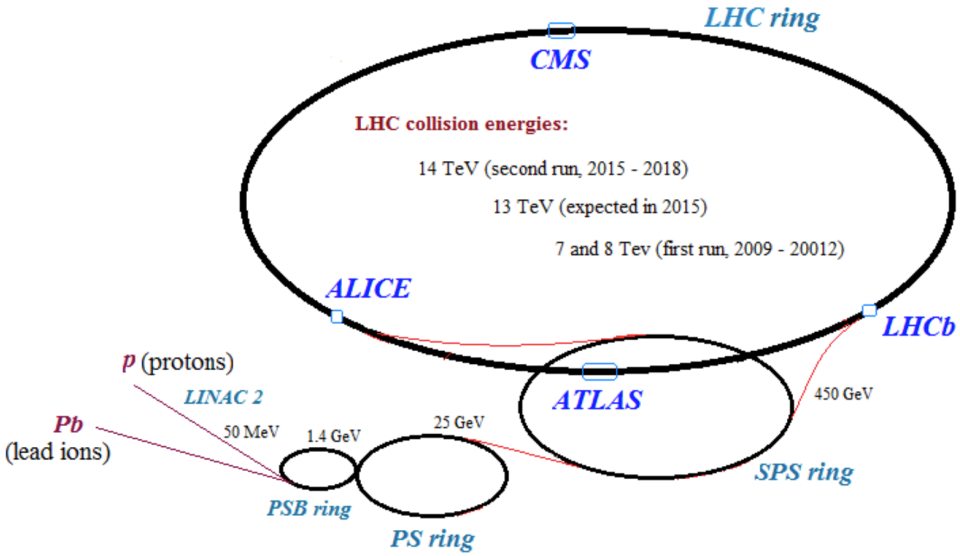

Figure 2.2: Scheme of the LHC accelerator complex [5]

The LHC physics programme is mainly based on proton–proton collisions with the largest center-of-mass energy in the world, with a maximal planned energy of 14 TeV and current energy of 13 TeV. There are approximately 2800 bunches at the same time along the ring, with approximately 10^{11} protons present in each bunch. Bunches flow through two separate magnetic channels, which only intersect in four places, where the four experiments are situated. The protons currently collide 40×10^6 times per second. The number of colliding particles and the frequency of their collisions can be summed in the instantaneous luminosity, which is a proportionality factor between cross-section of some process and number of events in which this process occurred. A related quantity is integrated luminosity, which is the integral of the luminosity with respect to time. The current integrated luminosity at LHC is 35.9 fb^{-1}, expected to reach 100 fb^{-1} by the end of data taken [18].

2.2 CMS Detector

The Compact Muon Solenoid (CMS) experiment is a general-purpose particle physics detector built on the Large Hadron Collider (LHC) [19, 20]. The goal of CMS experiment is to investigate a wide range of physics, including the search for the Higgs boson, extra dimensions and particles that could make up dark matter.

Its structure is summarized in Fig.2.3 below [21].

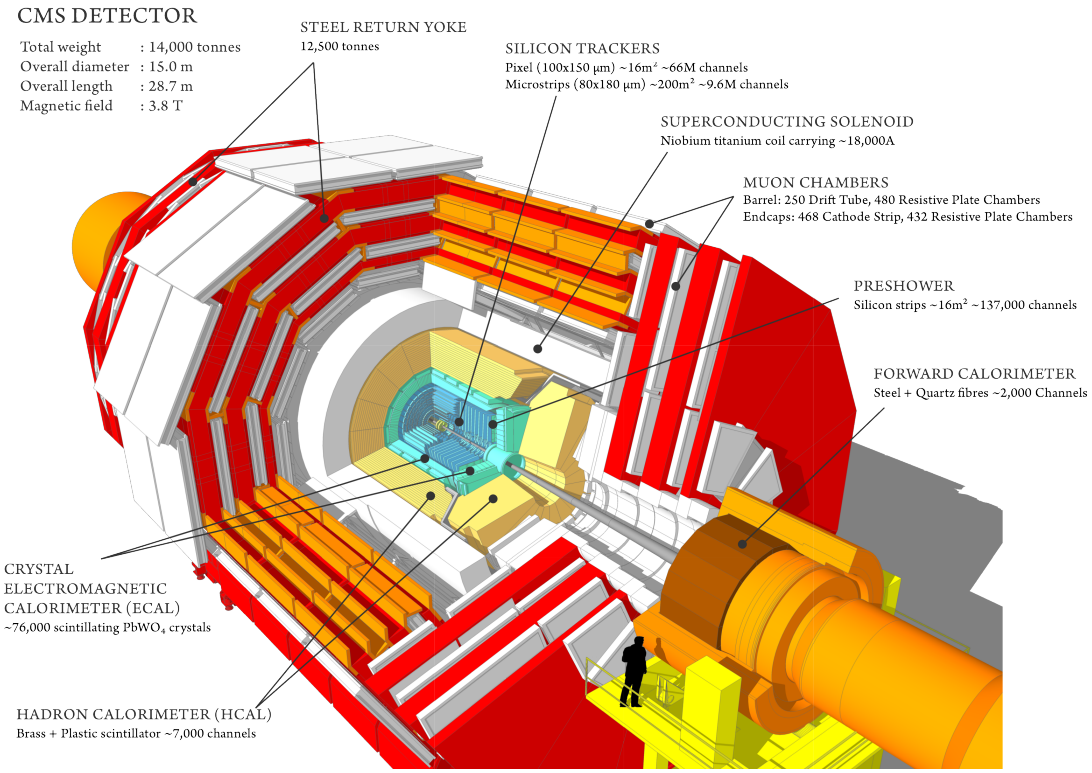

Figure 2.3: Scheme of the CMS detector and its main components [21].

The CMS detector is built around a huge solenoid magnet. This takes the form of a cylindrical coil of superconducting cable that generates a magnetic field of 4 teslas. It contains subsystems which are designed to measure the energy and momentum of photons, electrons, muons, and other products of the collisions [8]. The innermost layer is a silicon-based tracker. Surrounding it is a scintillating crystal electromagnetic calorimeter, which is itself surrounded with a sampling calorimeter for hadrons. The tracker and the calorimetry are compact enough to fit

inside the CMS solenoid. Outside the magnet are the large muon detectors, which are inside the return yoke of the magnet.

2.2.1 The magnet

The central feature of the CMS design is a large superconducting solenoid magnet [27]. It delivers an axial and uniform magnetic field of 3.8 T over a length of 12.5 m and a radius of 3.15 m. This radius is large enough to accommodate the tracker and both the electromagnetic and hadronic calorimeter, minimizing the amount of material in front of the calorimeters. This feature eliminates the energy losses before the calorimeters caused by particles showering in the coil material and facilitates the link between tracks and calorimeter clusters.

The job of the big magnet is to bend the paths of particles emerging from high-energy collisions in the LHC. The more momentum a particle has, the less its path is curved by the magnetic field, so tracing its path gives a measure of momentum. CMS began with the aim of having the strongest magnet possible because a higher strength field bends paths more and, combined with high-precision position measurements in the tracker and muon detectors, this allows accurate measurement of the momentum of even high-energy particles.

2.2.2 The silicon inner tracker

The tracker [22, 23] is the closest detector to the beamline, and is mainly responsible for reconstruction of tracks and vertices. It covers the central region with $|\eta| < 2.5$ and is made up of two sub-detectors. The first is Pixel detector, which is the innermost detector with the biggest granularity in order to handle the large multiplicities present in the area. It has two parts, a barrel with three layers and end-caps, where each cap has two layers. The outer detector is called Silicon Microstrip detector. Its inner part has four barrels and three end-cap layers, while the outer one has six barrels and nine disc layers. Each layer is either one-sided, providing 2D information about a hit, or double-sided, enabling 3D reconstruction.

Momentum of particles is crucial in helping us to build up a picture of events at the heart of the collision. One method to calculate the momentum of a particle is to track its path through a magnetic field; the more curved the path, the less momentum the particle had. The CMS tracker records the paths taken by charged

particles by finding their positions at a number of key points. The tracker can reconstruct the paths of high-energy muons, electrons and hadrons as well as see tracks coming from the decay of very short-lived particles. As particles travel through the tracker the pixels and microstrips produce tiny electric signals that are amplified and detected.

2.2.3 The electromagnetic calorimeter

The Electromagnetic calorimeter (ECal) [24, 25] is a hermetic homogeneous calorimeter made of lead tungstate (PbWO4) crystals. This is an extremely dense but optically clear material, ideal for stopping high energy particles. Lead tungstate crystal is made primarily of metal and is heavier than stainless steel, but with a touch of oxygen in this crystalline form it is highly transparent and scintillates when electrons and photons pass through it. This means it produces light in proportion to the particle's energy.

It consists of a barrel and two end-caps: the barrel covers $|\eta| < 1.5$ and the two endcap disks $1.5 < |\eta| < 3.0$. The barrel and endcap crystal length is sufficient to contain more than 98 % of the energy of electrons and photons up to 1 TeV. The fine transverse granularity makes it possible to fully resolve hadron and photon energy deposits, for the benefit of exclusive particle identification in jets. A much finer-grained detector, known as preshower, is installed in front of each endcap disk. It consists of two layers, each comprising a lead radiator followed by a plane of silicon strip sensors. These allow CMS to distinguish between single high-energy photons and the less interesting close pairs of low-energy photons.

2.2.4 The hadronic calorimeter

The hadronic calorimeter [26] is a hermetic sampling calorimeter consisting of several layers of brass absorber and plastic scintillator tiles, read out via wavelength-shifting fibres by hybrid photodiodes. This combination was determined to allow the maximum amount of absorbing material inside of the magnet coil.

It surrounds the electromagnetic calorimeter, with a barrel ($|\eta| < 1.3$) and two endcap disks ($1.3 < |\eta| < 3.0$). The barrel is made of two half-barrels covering positive and negative z, respectively. The high pseudorapidity region ($3.0 < |\eta| < 5.0$) is instrumented by the Hadronic Forward (HF) detector. This uses a slightly

different technology of steel absorbers and quartz fibres for readout, designed to allow better separation of particles in the forward region. Finally, the Hadronic Outer (HO) detector helps to contain central showers and is located outside of the magnet. The HO material is used as an additional absorber.

The Hadron Calorimeter (HCAL) measures the energy of hadrons, particles made of quarks and gluons. Additionally it provides indirect measurement of the presence of non-interacting, uncharged particles such as neutrinos.

2.2.5 The muon detectors

As the name "Compact Muon Solenoid" suggests, detecting muons is one of CMS's most important tasks [28]. Because muons can penetrate several metres of iron without interacting, unlike most particles they are not stopped by any of CMS's calorimeters. Therefore, chambers to detect muons are placed at the very edge of the experiment where they are the only particles likely to register a signal.

Outside the solenoid coil, the magnetic flux is returned through a yoke consisting of three layers of steel interleaved with four muon detector planes. To identify muons and measure their momenta, CMS uses three types of detector: drift tubes (DT), cathode strip chambers (CSC) and resistive plate chambers (RPC). The DTs are used for precise trajectory measurements in the central barrel region, while the CSCs are used in the end caps. The RPCs provide a fast signal when a muon passes through the muon detector, and are installed in both the barrel and the end caps.

Drift tube (DT) chambers and cathode strip chambers (CSC) detect muons in the regions $|\eta| < 1.2$ and $0.9 < |\eta| < 2.4$, respectively, and are complemented by a system of resistive plate chambers (RPC) covering the range $|\eta| < 1.6$. The reconstruction involves a global trajectory fit across the muon detectors and the inner tracker.

Chapter 3

Event Reconstruction

At a hadron collider one of the most important goals is the reconstruction of physics objects based on the signal collected by the detector and the ability to distinguish between various particles. Jets consist of hadrons and photons, the energy of which can be inclusively measured by the calorimeters without attempt to separate individual jet particles. Jet reconstruction can therefore be performed without any contribution from the tracker and the muon detectors. The same argument applies to the missing transverse momentum reconstruction.

The reconstruction of isolated photons and electrons concerns the electromagnetic calorimeter. The tagging of jets originating from b quark hadronization is based on the properties of the charged particle tracks and involves the tracker. The identification of muons is principally based on the information from the muon detectors [8].

A significantly improved event description can be achieved by correlating the basic elements from all detector layers to identify each final-state particle, and by combining the corresponding measurements to reconstruct the particle properties on the basis of this identification. This approach is called particle-flow (PF) reconstruction.

3.1 Particle-flow reconstruction

The particle-flow algorithm is employed to reconstruct and identify each individual particle with a combination of information from the various elements of the CMS detector. The algorithm identifies each reconstructed particle either as an electron, a muon, a photon, a charged hadron, or a neutral hadron. These particles are then used to build higher-level physics objects, such as jets, and the missing transverse momentum, with superior resolution. The particle-flow algorithm is not responsible only for the identification of the particles, as was already mentioned, but also for giving the best estimate of particle properties.

Key ingredients for the success of particle-flow are excellent tracking efficiency and purity, the ability to resolve the calorimeter energy deposits of neighbouring particles, and unambiguous matching of charged-particle tracks to calorimeter deposits. The CMS detector, while not designed for this purpose, turned out to be well-suited for particle-flow.

Starting from the beam interaction region, particles first enter a tracker, in which charged-particle trajectories (tracks) and origins (vertices) are reconstructed from signals (hits) in the sensitive layers.

The tracker is inside a magnetic field that bends the trajectories and allows the electric charges and momenta of charged particles to be measured. Electrons and photons are then absorbed in an electromagnetic calotimeter. The corresponding electromagnetic showers are detected as clusters of energy recorded in neighbouring cells, from which the energy and direction of the particles can be determined.

Charged and neutral hadrons may initiate a hadronic shower in the electromagnetic calorimeter, which is subsequently absorbed in the hadron calorimeter. The corresponding clusters are used to estimate their energies and directions.

Muons and neutrinos traverse the calorimeters with little or no interactions. While neutrinos escape undetected, muons produce hits in additional tracking layers called muon detectors, located outside the calorimeters [8].

This view is graphically summarized in Fig. 3.1, which displays a sketch of a transverse slice of the CMS detector [8].

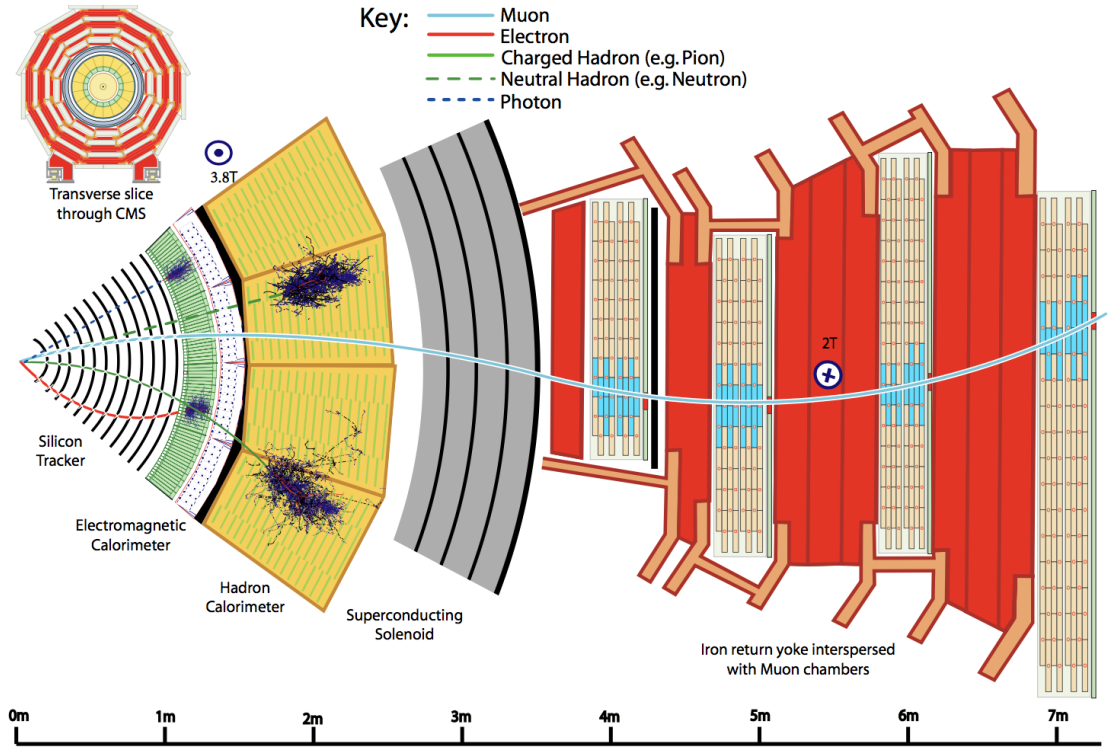

Figure 3.1: A sketch of the specific particle interactions in a transverse slice of the CMS detector, from the beam interaction region to the muon detector [8].

The presence of a charged hadron is signalled by a track connected to calorimeter energy deposits. The direction of the particle is indicated by the track before any deviation in the field, and its energy is calculated as a weighted average of the track momentum and the associated calorimeter energy. These particles, which typically carry about 65% of the energy of a jet, are therefore reconstructed with the best possible energy resolution. Calorimeter energy deposits not connected to a track are either identified as a photon or as a neutral hadron. Photons, which represent typically 25% of the jet energy, are reconstructed with the excellent energy resolution of the CMS electromagnetic calorimeter. Consequently, only 10% of the jet energy – the average fraction carried by neutral hadrons – needs to be reconstructed using the hadron calorimeter. In addition to these types of particles, the algorithm identifies and reconstructs leptons with improved efficiency and purity [29].

Charged-particle tracks are reconstructed with efficiency greater than 90% and a rate of false track reconstruction at the per cent level. Excellent separation of charged hadron and photon energy deposits is provided by the granular electromagnetic calorimeter and large magnetic-field strength. Finally, the two calorimeters are placed inside of the magnet coil, which minimises the probability for a charged particle to generate a shower before reaching the calorimeters, and therefore facilitates the matching between tracks and calorimeter deposits [29].

3.2 Jet reconstruction: the anti-k_t algorithm

The particle-flow candidates are clustered into jets using the anti-k_t algorithm. It belongs to the class of sequential recombination jet algorithms and it is parametrized by the power of energy scale in the distance measure. The distance measures are defined using the transverse momentum, rapidity and the azimuth of the particle. This anti-k_t algorithm essentially behaves like an idealised cone algorithm: in fact there is also the radius parameter R, which can be identified as the radius of the reconstructed idealised cone. The R parameter is important because it defines the new strategy to reconstruct the Higgs jet. In the end, there is a new parameter added p used to govern the power of the energy. The p parameter is negative and from this value comes the name of "anti-k_t" [6].

As usual, one introduces distances d_{ij} between entities (particles, pseudojets) i and j and d_{iB} between entity i and the beam (B). The clustering proceeds by identifying the smallest of the distances and if it is a d_{ij} recombining entities i and j, while if it is d_{iB} calling i a jet and removing it from the list of entities. The distances are recalculated and the procedure repeated until no entities are left. The distance measures are defined as follows:

$$d_{ij} = min(k_{ti}^{2p}, k_{tj}^{2p}) \frac{\Delta_{ij}^2}{R^2} \tag{3.1}$$

$$d_{iB} = k_{ti}^{2p} \tag{3.2}$$

where

$$\Delta_{ij}^2 = (y_i - y_j)^2 + (\Phi_i - \Phi_j)^2 \tag{3.3}$$

and k_{ti}, y_i and Φ_i are respectively the transverse momentum, rapidity and azimuth of particle i. In addition to the usual radius parameter R, we have added a parameter p to govern the relative power of the energy. Negative values of p might at first sight seem pathological. The behaviour with respect to soft radiation will be similar for all $p < 0$, so here $p = -1$, and refer to it as the "anti-k_t" jet-clustering algorithm [6].

3.3 Identification of b-quarks

The identification or "b-tagging" of jets resulting from fragmentation and hadronization of bottom quarks is an important part of high-p_t collider physics. The ability to identify b-jets accurately plays a fundamental role in reducing the otherwise overwhelming background to these signatures from processes involving jets from gluons (g) and light-flavor quarks (u, d, s).

A variety of reconstructed objects - tracks, vertices, identified leptons - are used to build observables, which are then combined into a discrimination variable separating b from light-flavor jets.

3.3.1 B Hadrons properties

Jets containing B hadrons have distinctive properties that are useful in distinguishing them from other types of jets.

A useful property of B hadrons in this respect is their long lifetime, with $c\tau \sim 500$ μm. A B hadron with $p_t = 50$ GeV will fly on average almost half centimeter ($L \sim \gamma c\tau$) before decaying. This translates into the fact that daughter particles can have a sizable impact parameter with respect to the B hadron point of origin. The impact parameter $d \sim Lsin(\alpha) \sim \gamma c\tau\alpha \sim c\tau$ is boost invariant, where α is the average opening angle of the decay products.

The fragmentation process of b quarks into B hadrons cannot be fully described at the perturbative level, and must therefore rely on phenomenological models.

The B hadrons are much more massive than anything they decay into, thus the decay products have order of a GeV of momentum in the B rest frame. These particles also have high p_t relative to the beam axis, which reduces the effects of multiple scattering and allows these impact parameters to be measured with good resolution.

3.3.2 Tracks selection

The B-hadron properties cause the b-jets to be wide, characterized by high track multiplicity and large invariant mass.

In the B decay chain an additional "tertiary" vertex resulting from the s-quark decay, can be reconstructed. These vertices may have only one reconstructed track, which is not necessarily compatible with the secondary vertex.

Tracks from a B hadron decay are typically produced with an impact parameter with respect to the interaction point (see Fig.3.2).

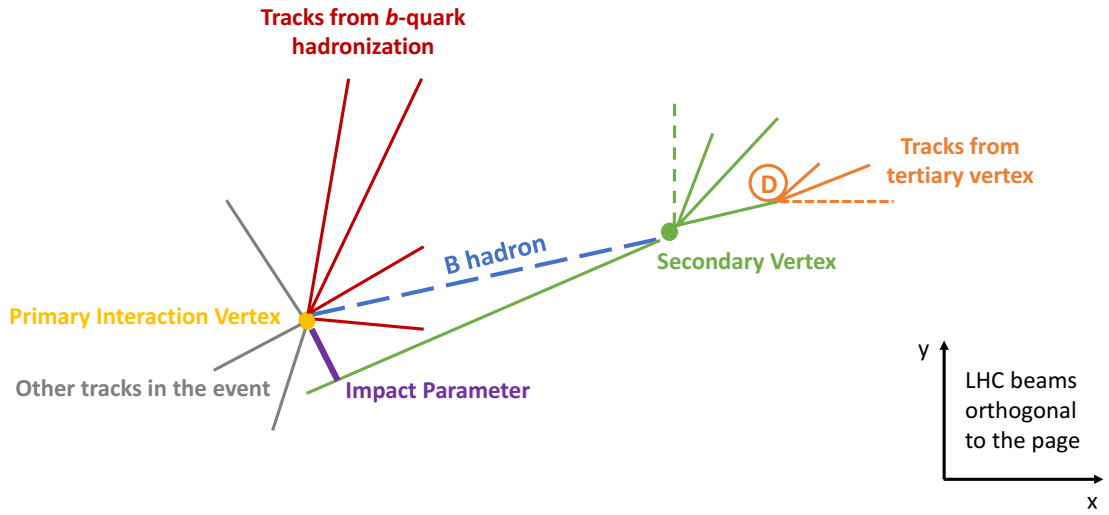

Figure 3.2: Schematic summary of the properties used to identify a B hadron decay.

Since tracks from B hadron decays are mostly produced in a cone in the B hadron flight direction, one can approximate the B hadron flight direction with the jet direction and then search for tracks in the jet cone (See Fig.3.3 below [1]).

The fraction of fake or poorly reconstructed tracks is reduced by requiring a transverse momentum of at least 1 GeV, at least eight hits associated to the

track and a good fit quality. Since the track measurements in the vicinity of the interaction vertex contain most of the discriminating power, at least two hits are required in the pixel system to ensure a good resolution for the impact parameter measurement. A loose selection on the transverse track impact parameter is used to further increase the purity and to reduce the contamination from decay products of long-lived particles.

In order to minimize the combinatorial complexity in the reconstruction of secondary vertices, which is more challenging in the presence of the multiple proton-proton interactions, a more restrictive track selection is applied. A vertex candidate is identified by applying an adaptive vertex fit, which estimates the vertex position and weights each track according to its compatibility with the vertex.

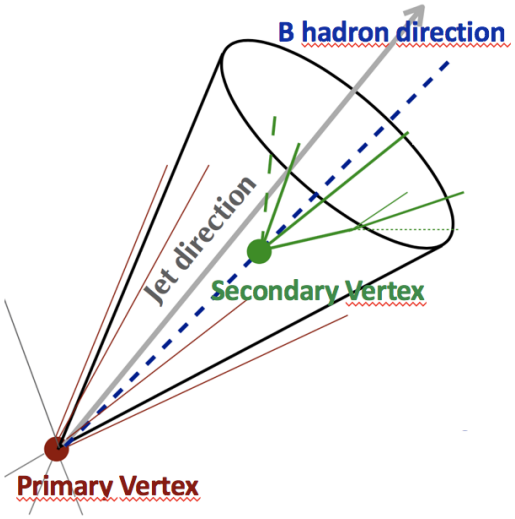

Figure 3.3: Scheme of the B hadron decay tracks and the jet direction [1].

3.3.3 *b*-tagging observables

The main observables used as an input to the *b*-tagging algorithms are related to the B hadron lifetime and the presence of a secondary vertex. The impact parameter (IP) of a track with respect to the primary vertex can be used to distinguish decay products of a B hadron from prompt tracks. The impact parameter is calculated in three dimensions, taking advantage of the excellent resolution of the pixel detector.

The impact parameters are signed according to the scalar product of the vector pointing from the primary vertex to the point of closest approach with the jet direction: tracks originating from the decay of particles travelling along the jet axis will tend to have positive IP values while the impact parameters of prompt tracks can have positive or negative signs. The resolution on the impact parameter depends strongly on p_t and η of a track.

The presence of a secondary decay vertex and kinematic variables associated with this vertex can be used to discriminate between b and non-b jets. These variables include the flight distance and direction, i.e. the vector between primary and secondary vertex, and various properties of the system of associated secondary tracks such as the multiplicity, the mass or the energy.

3.4 Higgs-jet reconstruction

The angular distance between the two b-jets coming from the Higgs decay can be calculated as:

$$dR(b\bar{b}) \sim \frac{m_H}{p_t} \tag{3.4}$$

where m_H is the Higgs mass (125 GeV) and p_t is its transverse momentum.

If we consider a Higgs boson with low p_t, the angular distance $dR(b\bar{b})$ is big enough to reconstruct two separate b-jets (Fig.3.4a). In this search, we are requiring a high transverse momentum Higgs, thus the angular distance $dR(b\bar{b})$ is too small to reconstruct the two b-jets separately.

Then the strategy to reconstruct the Higgs jet is to consider one single large-cone (fat) jet with $R = 0.8$ (Fig.3.4b) instead of taking two separate b-jets with $R = 0.4$ for the two quarks [1]. Therefore the decay products of a high-p_t $H \to b\bar{b}$ system are reconstructed as one AK8 jet.

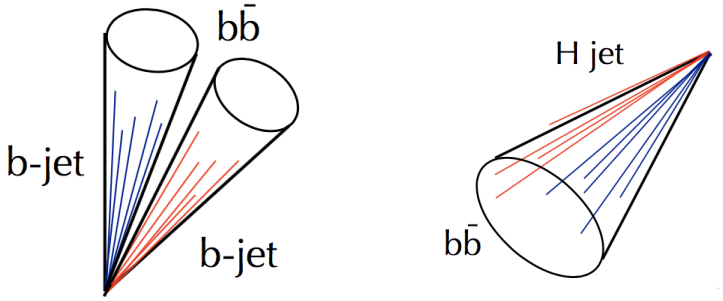

(a) (b)

Figure 3.4: ***Higgs-jet reconstruction methods***
(a): Two separate b-jets: $R = 0.4$.
(b): One single large cone jet (fat jet): $R = 0.8$.

There are different tools for identifying $H \to b\bar{b}$ signal at high trasverse momentum: double-b tagging to reconstruct the two B hadrons from the b and $\bar{b}$ within the same fat jet; jet mass compatibility with the Higgs; the composite nature of the jet using substructure.

3.4.1 Double-b tagger

The technique used to identifying the b jets coming from the Higgs boson decay is the Double-b tagger. It identifies the two B hadron decay chains from b and $\bar{b}$ quarks within the same fat jet (See Fig.3.5) [1].

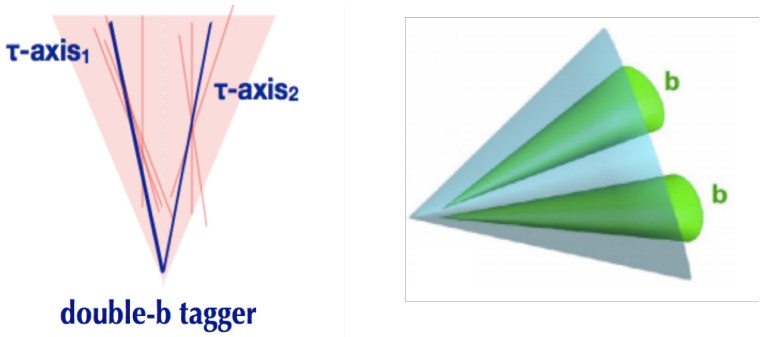

Figure 3.5: Scheme of the Double-b tagging principle.

The Double-b tagger combines tracking and vertexing information with a multivariate approach. It targets the $b\bar{b}$ signal aiming to be mass indipendent and p_t indipendent.

3.4.2 Jet soft drop mass

Here it is used a tagging/grooming method called soft drop declustering. Like any grooming method, soft drop declustering removes wide-angle soft radiation from a jet in order to mitigate the effects of contamination from initial state radiation (ISR), underlying event (UE), and multiple hadron scattering (pileup). Given a jet of radius R_0 with only two constituents, the soft drop procedure removes the softer constituent unless:

$$\frac{min(p_{t1}, p_{t2})}{p_{t1} + p_{t2}} > z_{cut}\left(\frac{\Delta R_{12}}{R_0}\right)^{\beta} \tag{3.5}$$

where p_{ti} are the transverse momenta of the constituents with respect to the beam, ΔR_{12} is their distance in the rapidity-azimuth plane, z_{cut} is the soft drop threshold, and β is an angular exponent. By construction, Eq.3.5 fails for wide-angle soft radiation. The degree of jet grooming is controlled by z_{cut} and β, with $\beta \to \infty$ returning back an ungroomed jet [7].

For $\beta > 0$, soft drop declustering removes soft radiation from a jet while still maintaining a fraction (controlled by β) of the soft-collinear radiation. For $\beta < 0$, soft drop declustering can remove both soft and collinear radiation.

For a jet to pass the soft drop procedure, it must have at least two constituents satisfying Eq.3.5. Thus, in this regime, soft drop acts like a "tagger", since it vetoes jets that do not have two well-separated hard prongs.

The soft drop declustering procedure depends on two parameters, a soft threshold z_{cut} and an angular exponent β, and is implemented as follows:

1. Break the jet j into two subjets. Label the resulting two subjets as j_1 and j_2.

2. If the subjets pass the soft drop condition Eq.3.5, then deem j to be the final soft-drop jet.

3. Otherwise, redefine j to be equal to subjet with larger p_t and iterate the procedure (See Fig.3.6 [1]).

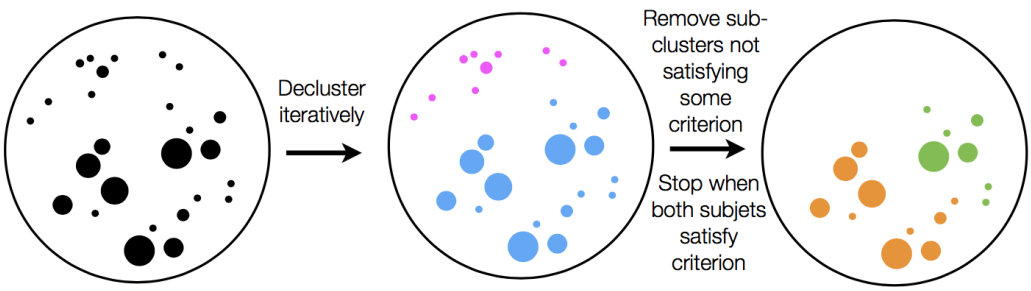

Figure 3.6: Scheme of the soft drop declustering method [1].

This algorithm helps to get the true mass and eliminate the extra particles not coming from the original jet. The soft drop jet mass m_{SD} peaks at the Higgs boson mass for signal events and reduces the masses of jets from background.

The distribution of the jet soft drop mass is p_t-dependent. Thus, we define a variable whose shape is p_t-independent: the "scaling" variable ρ. The "scaling" variable for QCD jets ρ is defined as:

$$\rho = log\left(\frac{m_{SD}^2}{p_t^2}\right) \tag{3.6}$$

3.4.3 Jet substructure

The jet substructure measures the degree to which a jet can be considered as composed of N prongs. The energy correlation functions E are sensitive to N-point correlations in a jet. For a two-pronged structure (Fig.3.7 [1]), signal jets have a stronger 2-point correlation than a 3-point correlation, i.e. $E_3 < E_2$. In the case here, it's expected to have 2 prongs, one for every b quark of the process, thus the variable N_2 can be defined as follows:

$$N_2 = \frac{E_3}{(E_2)^2} \tag{3.7}$$

where E_3 is the energy correlation function for a 3-pronged structure and E_2 is the energy correlation function for a 2-pronged structure.

This variable, which is based on the ratio of 2-point and 3-point generalized energy correlation functions, is exploited to determine how consistent a jet is with having a two-prongs substructure [2].

The N_2 observable provides excellent performance in discriminating two-prongs signal jets from QCD background jets. However, N_2 and many others similar variables are correlated with the jet mass and p_t. The decorrelation procedure uses simulated QCD events and defines:

$$N_2^{DDT} = N_2 - N_2^* \tag{3.8}$$

where N_2^* is the value calculated at 26 % of QCD efficiency. This ensures that the selection on N_2^{DDT}, applied in the next chapter, yields a constant QCD background efficiency of 26% across the whole ρ and p_t range considered in this search [2].

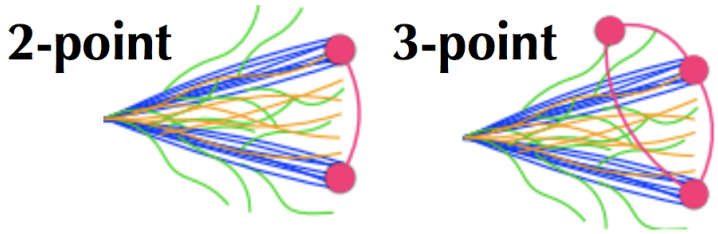

Figure 3.7: Substructure of a 2-pronged jet [1].

Chapter 4

Event selection

The focus of this report is the search for $H \to b\bar{b}$ in the ggF production mode with the requirement of a high transverse momentum Higgs. In this search, the main target of my work was to contribute to the optimization of the event selection by analyzing the discrimination between ggF and VBF production mode and to find some observables through which it is possible to separate the two processes. Therefore, we select the events according to the values of different variables.

4.1 Gluon Fusion and Vector Boson Fusion

As just said in the previous section, the dominant contribution for the production of a Higgs boson comes from the gluon fusion production mode. It was considered impossible to observe and measure, but recently it has been proved to be possible requiring a high transverse momentum Higgs. For this reason, my work focused on this process. Besides the dominant gluon fusion process, other production mechanisms contribute to the SM Higgs boson signal. Therefore, the main target of my work was to find some observables through which it is possible to separate the gluon fusion events from the vector boson fusion contribution.

The Vector Boson Fusion process is the second most important contribution. In order to distinguish the gluon fusion production mode from this process, we have to explain the topology of the Vector Boson Fusion. The scheme of this process is shown in Fig.4.1 below.

In this process, the Higgs boson is produced by the fusion of two vector bosons

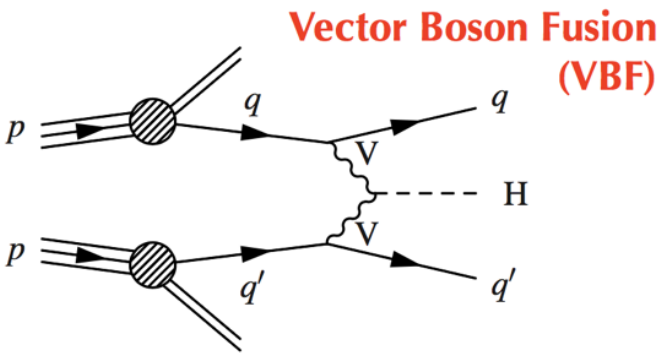

Figure 4.1: The Vector Boson Fusion production mode (VBF)

(W or Z). The Vector Boson Fusion has a very distinctive topology [3]. The prominent feature of the VBF process is the presence of four energetic jets in the final state. Two jets are expected to originate from a light-quark pair (u or d), which are typically two valence quarks from each of the colliding protons scattered away from the beam line in the VBF process. These "VBF-tagging" jets are expected to be roughly in the forward and backward directions relative to the beam direction with large pseudorapidity. Two additional jets are expected from the Higgs boson decay to a $b\bar{b}$ pair in more central regions of the detector.

Another important property of the signal events is that, being produced through an electroweak process, no quantum chromodynamics (QCD) color is exchanged at leading order in the production. As a result, the VBF-tagging jets connect to the proton remnants in the forward and backward beam line directions, while the two b-quark jets connect to each other as decay products of the color neutral Higgs boson. Consequently very little additional QCD radiation and hadronic activity is expected [3].

4.2 Kinematic selections

To isolate the Higgs boson signal in the gluon fusion process, a high-p_t signal jet is required. Combinations of several online selections are used, all requiring the total hadronic transverse energy in the event H_T (Eq.4.1) or jet p_t to be above a given threshold. Extra requirements on the jet mass after removing remnants of soft radiation are added to reduce the H_T or p_t thresholds in order to improve signal acceptance [2]. The online selection is fully efficient at selecting events offline with at least one AK8 jet with $p_t > 450$ GeV and $|\eta| < 2.5$. The transverse momentum of the Higgs jet has to be greater than 450 GeV because at lower p_t it's not possible to have an online selection that allows to register events with only one jet.

$$H_T = \sum_{i}^{jets} \left| \vec{p_T}, i \right| \tag{4.1}$$

As said in Sec.3.4.2, the soft drop algorithm is used to remove soft and wide-angle radiation. Here we select the soft radiation fraction z_{cut} greater than 0.1 and angular exponent parameter of $\beta = 0$. The soft drop mass of the Higgs jet has to be greater than 40 GeV because expecting a Higgs with a mass around 125 GeV, the events at lower mass with much more background are not relevant.

We have to make some selections also on the "scaling" variable ρ (defined in Sec.3.4.2). Only events in the ρ range $-6.0 < \rho < -2.1$ are considered, to avoid instabilities at the edges of the distribution due to finite cone effects from the AK8 jet clustering (around $\rho \sim -2$), and to avoid the non-perturbative regime of the soft drop mass calculation (below $\rho \sim -6$). This requirement is fully efficient for the Higgs boson signal [2].

Events containing identified and isolated electrons, muons, or taus with $p_t > 10$ GeV and $|\eta| < 2.5$ are vetoed to reduce backgrounds from the electroweak processes. Since no real missing energy (E_T^{miss}) is expected for signal events, events with E_T^{miss} > 140 GeV are removed in order to further reduce top background contamination from $t\bar{t}$ [2].

4.3 Higgs candidate selection

In order to select events for which the H jet is most likely to contain two b quarks, the double-b tagger algorithm is used. The double-b tagger aims to fully exploit the presence of two b quarks inside an AK8 jet and their topology in relation to the jet substructure. Several observables exploiting the distinctive properties of B hadrons are used as input variables to a multivariate algorithm, to distinguish between the H jet and the background from QCD jets. Events are selected by requiring the double-b tag discriminator value be greater than 0.9 (Fig.4.2 [1]), which corresponds to about 1% efficiency for QCD jets and 33% for $H \to b\bar{b}$ signal [2]. This value has been optimized to maximize the sensitivity of the search. Events are categorized depending on whether the jet has a double-b tag discriminator value greater than 0.9 (passing region) or not (failing region).

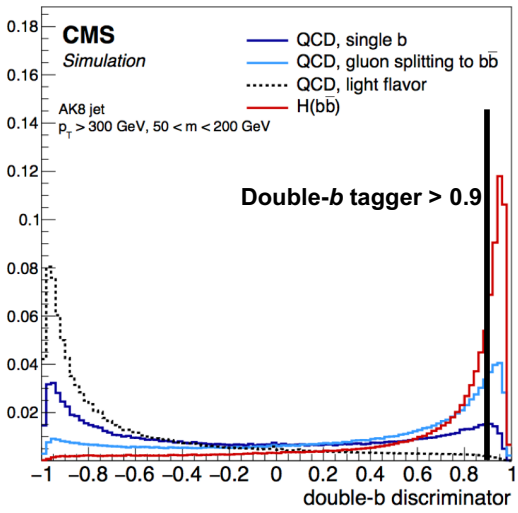

Figure 4.2: Selection on the double-b tag discriminator [1].

Moreover, there is a selection also on the jet substructure variable N_2^{DDT} defined in Sec.3.4.3. The selection required on this variable is $N_2^{DDT} < 0$.

4.4 Additional jets selection

In order to distinguish between the Gluon Fusion and the Vector Boson Fusion processes, we make some selections also on the two jets originating from quarks in the Vector Boson Fusion (see Sec.4.1).

They are tighter than the Higgs jet, thus they are reconstructed with the same anti-k_t algorithm but with the distance parameter $R = 0.4$. For this reason, they are called AK4 jets.

All the AK4 jets found in an event are ordered according to their p_t and the q-jet candidates are searched among the six leading ones. In order to select the most probable jets coming from the quarks, it's necessary to make some selections: the transverse momentum of the AK4 jet is required to be greater than 30 GeV, $p_t > 30$ GeV, and the modulus of the pseudorapidity has to be less than 2.5, $|\eta| < 2.5$.

In the end, in order to be sure that these AK4 jets are not overlapped with the Higgs jet, the angular distance dR defined as:

$$dR(AK4, AK8) = \sqrt{(\Delta\eta)^2 + (\Delta\Phi)^2} \tag{4.2}$$

has to be greater than 0.3.

4.5 Quark/gluon jets selection

In the vector boson fusion process, the signal jets are originating from quarks, while jets in the background are more gluon enriched. Based on observables sensitive to fundamental differences in the fragmentation properties of gluons and quarks, a discriminant is constructed to distinguish between jets originating from quarks and gluons.

Because of different colour interaction and hadronization, gluon jets are wider, with higher multiplicities and have a more uniform energy fragmentation, while quark jets are more likely to produce narrow jets with hard constituents that carry a significant fraction of the energy [10].

4.5.1 Quark/gluon discriminant

The quark-gluon discriminant makes use of these jet properties through variables provided by the CMS particle-flow reconstruction. It defines a probability between 0 and 1: if the discriminant value is near 1, the jet is probable to come from a quark; if the discriminant value is near 0, the jet is probable to come from a gluon [10].

Three variables are chosen to build a discriminator:

- The multiplicity, i.e. the total number of particle flow candidates reconstructed within the jet.
- The jet energy sharing variable:

$$p_{t,D} = \frac{\sqrt{\sum_i p_{t,i}^2}}{\sum_i p_{t,i}} \tag{4.3}$$

  which has $p_{t,D} \to 1$ for jets made of only one particle that carries all of its momentum and $p_t\mathrm{D} \to 0$ for a jet made of an infinite number of particles.
- The angular spread measured in $\eta - \Phi$ plane.

A better discrimination power is found by restricting the charged particle flow candidates to those linked to tracks compatible with the primary interaction vertex [10].

4.5.2 Quark/gluon likelihood ratio

In order to distinguish between gluon fusion and vector boson fusion production mode, we use the quark/gluon discriminant of a single jet (defined in the previous section) to construct a discriminant for the whole event: this is the quark/gluon likelihood ratio. As just said, the quark/gluon discriminant gives the probability that a jet comes from a quark or a gluon, with quark-like jets having a value near 1 and gluon-like jets having a value near 0, but the quark/gluon likelihood ratio (QGLR) could lead to a better discrimination because it defines the probability that the whole event contains two quark jets instead of having only the probability of the single jet to come from a quark or a gluon. Thus the information given from QGLR is bigger and more precise [9].

It works best for light-flavor jets as b jets tend to have similar properties to gluon jets and thus have quark/gluon discriminant values closer to 0 than 1.

The QGLR for an event is defined as follows:

$$q_{LR(QvA)} = \frac{L(Qq, 0g)}{L(Qq, 0g) + L(Aq, (Q-A)g)} \tag{4.4}$$

where the individual likelihoods are defined as:

$$L(Qq, Gg) = \sum_{i_1} \sum_{i_2 \neq i_1} \cdots \sum_{i_{Q+G} \neq i_1, \ldots, i_{Q+G-1}} \left\{ \prod_{k \in \{i_1, \ldots, i_Q\}} f_q(\zeta_k) \prod_{m \in \{i_{Q+1}, \ldots, i_{Q+G}\}} f_g(\zeta_m) \right\} \tag{4.5}$$

where ζ_i is the QGL discriminator for the i-th jet, and f_q and f_g are the probability density functions (pdf) of ζ_i when the i-th jet originates from a quark or a gluon. $L(Qq, Gg)$ is the probability that Q jets are coming from Q quarks and G gluons [9].

The former include u, d, s, and c quarks, but not b quarks. The likelihood ratio on Eq.4.4 is suitable for discriminating light-flavor quarks from gluons and is thus used only for this purpose and does not include any jets previously identified as b jets in its calculation. The sums in Eq.4.5 run over all inequivalent permutations of assigning Q jets to quarks and G jets to gluons.

In this analysis, the QGLR is used to select events in the signal region, and thus need only to decide whether or not the light jets in an event come mostly from quarks or mostly from gluons. Specifically, it is compared the likelihood of the N light jets in an event coming from N quarks to the likelihood of the N light jets coming from N gluons.

Chapter 5

Analysis and Results

My work of analysis started making the plot of the soft drop mass distribution of the Higgs jet, m_{SD} distribution, after all the selection criteria (Fig.5.1) considering only the gluon fusion (ggF) and the vector boson fusion (VBF) processes. This because, as already said, the main target of my analysis was studying the gluon fusion process and trying to separate its contribution from the others (mainly from vector boson fusion).

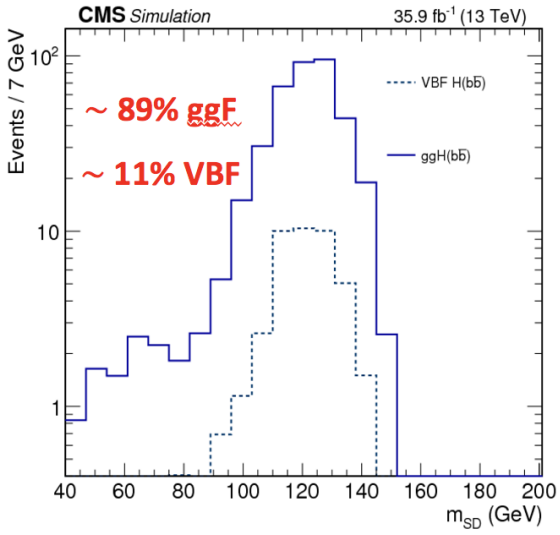

Figure 5.1: The m_{SD} distribution for simulated signal events after all the selection criteria, only for ggF and VBF

From Fig.5.1, you can see that ggF contributes with the 89% in the signal region, while the remaining 11% is from VBF.

I also performed another type of analysis using two-dimensional plots separately for gluon fusion and vector boson fusion. On the x axis there is the mass of the two jets with the highest values of the quark/gluon discriminant, i.e. the leading and the subleading AK4 jets, and on the y there is the $\Delta\eta$ of the two same jets. The distributions of the two processes are shown in Fig.5.2.

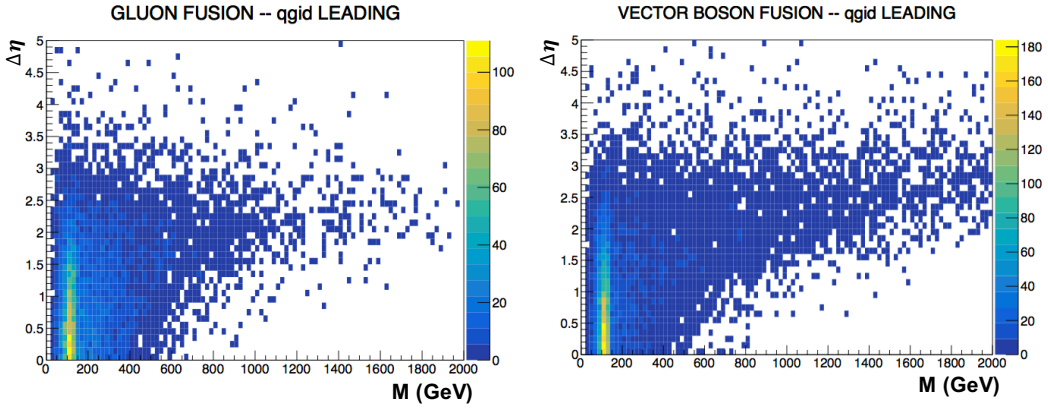

Figure 5.2: Two-dimensional distributions of quark/gluon discriminant for the leading jets.

From Fig.5.2 you can see the difference between the two processes: vector boson fusion has much more events with high mass and high pseodurapidity. Thus, the different topologies of the two processes can help to distinguish their contributions.

My most important task was to optimize the event selection in order to improve the analysis and enhance more the ggF contribution.

To do this, it's necessary to study better the discrimination between quark jets and gluon jets, using both the methods described in Sec.4.5.

After taking into account only the AK4 jets that passed the selections explained in the Sec.4.4, I calculated the quark/gluon discriminant for all these jets and I used this variable to sort them, from the jet with the biggest value of the quark/gluon discriminant to the jet with the smallest value of it. The Fig.5.3 shows the distribution of the quark/gluon discriminant for the subleading AK4 jet (the same distribution for the leading jet didn't show a visible distinction between ggF and VBF.) You can see that from 0.8 to 1 value of the quark/gluon discriminant

there is a difference of contributions of the two processes but the discrimination is very tiny.

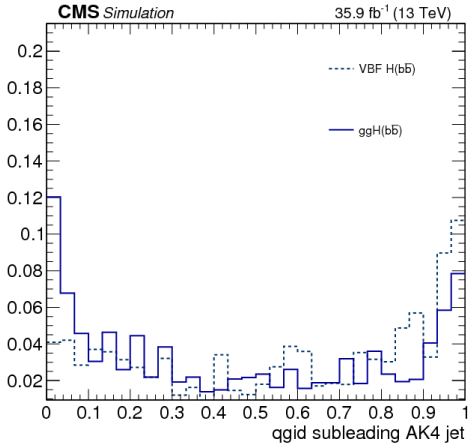

Figure 5.3: Quark/gluon discriminant distribution for subleading AK4 jet

Thus, I analyzed the quark/gluon likelihood ratio. The distribution for each event is shown in Fig.5.4, with the dR parameter defined in Eq.4.2 greater than 0.8 ($dR > 0.8$).

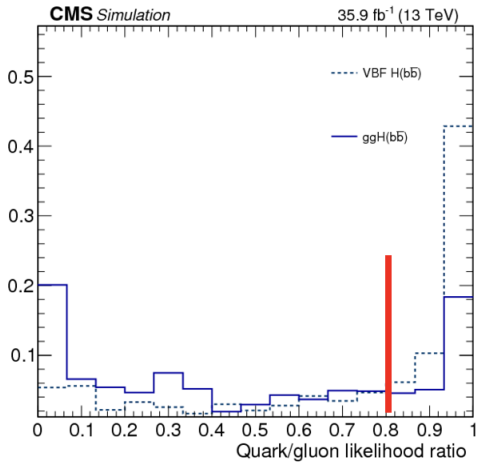

Figure 5.4: Distribution of quark/gluon likelihood ratio with $dR > 0.8$

From Fig.5.4, for QGLR < 0.8 you can start to see a discrimination between gluon fusion and vector boson fusion because the first process has a bigger contribution, but the distinction can be improved selecting a smaller value for the dR: it has to be grater than 0.3 instead of 0.8 ($dR > 0.3$: I tried a lot of different values before finding that this was the best cut). With this new value of dR, the distribution of the quark/gluon likelihood ratio changes as shown in Fig.5.5.

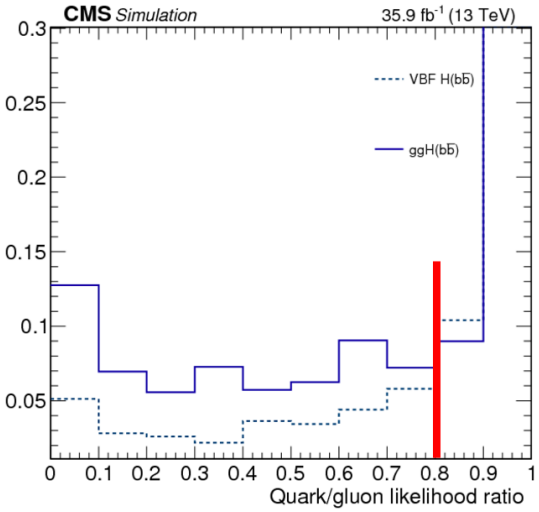

Figure 5.5: Distribution of quark/gluon likelihood ratio with $dR > 0.3$

From Fig.5.5, you can see a real distinction between the two processes and the discrimination is improved because the gluon fusion has a much bigger contribution with respect to the vector boson fusion and now the separation is very visible for QGLR < 0.8.

In the end, with this analysis on the quark/gluon likelihood ratio, I added the new cut on the quark/gluon variable to the selections previously explained in the Sec.4.

After the selection procedure, it's possible to see the new fractions of the contribution of the two processes to the mass distribution: Fig.5.6.

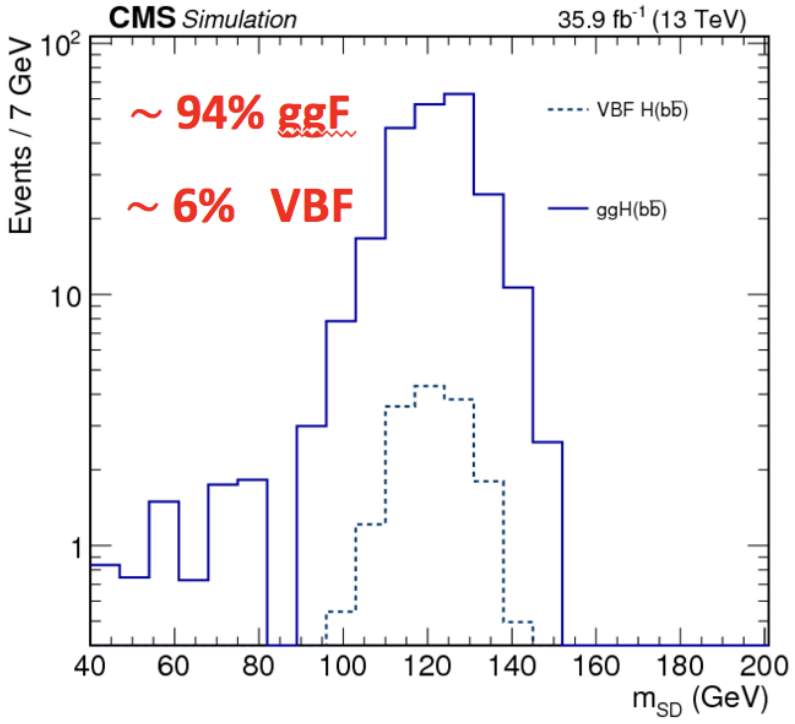

Figure 5.6: The m_{SD} distribution for simulated signal events after all the selection criteria, QGLR included.

The percentage of contribution of gluon fusion process is now 94% (almost the totality of the signal), with respect to the 89% of the Fig.5.1 without the QGLR cut. The improvement is remarkable. Now it's possible to better distinguish the gluon fusion process from the vector boson fusion process and this was the main goal of my analysis.

Chapter 6

Conclusions

A search for the standard model Higgs boson decaying to bottom quark-antiquark pairs with $p_t > 450$ GeV and reconstructed as a single jet has been presented using simulated signal events of proton-proton collisions in CMS corresponding to 35.9 fb^{-1} at $\sqrt{s} = 13$ TeV. The events are reconstructed using the CMS particle-flow algorithm. The Higgs jets are reconstructed with the anti-k_t algorithm with radius $R = 0.8$ and identified with the CMS double-b tag algorithm. The signal is then extracted using the soft drop mass declustering, studying the jet substructure and making selections on different variables. In the end, the improvement of the signal events is achieved developing a likelihood discriminant to separate jets originating from gluons or light-quarks. Thus, with my work, I contributed to the optimization of the event selection and improved the fractions of the contributions of gluon fusion and vector boson fusion processes to the mass distribution of the Higgs jet.

Bibliography

[1] C. Vernieri, "First experimental search for inclusive Higgs boson production using the $H \to b\bar{b}$ decay with CMS" (2017) `https://web.fnal.gov/organization/theory/JETP/2016/seminar-hbb-2017-wc-final`

[2] CMS Collaboration [CMS Collaboration], "Inclusive search for the standard model Higgs boson produced in pp collisions at $\sqrt{s} = 13$ TeV using H$\to$ b$\bar{\text{b}}$ decays," CMS-PAS-HIG-17-010.

[3] CMS Collaboration [CMS Collaboration], "Search for the standard model Higgs boson produced through vector boson fusion and decaying to b$\bar{\text{b}}$ with proton-proton collisions at $\sqrt{s} = 13$ TeV" CMS-PAS-HIG-17-021.

[4] CMS Collaboration [CMS Collaboration], "Search for the standard model Higgs boson produced in vector boson fusion and decaying to bottom quarks using the $\sqrt{s} = 13$ TeV 2016 data sample " CMS AN-17-106.

[5] N. A. Ky and N. T. H. Van, "Was the Higgs boson discovered?" arXiv:1503.08630 [hep-ph].

[6] M. Cacciari, G. P. Salam and G. Soyez, "The Anti-k(t) jet clustering algorithm" JHEP **0804**, 063 (2008) doi:10.1088/1126-6708/2008/04/063 [arXiv:0802.1189 [hep-ph]].

[7] A. J. Larkoski, S. Marzani, G. Soyez and J. Thaler, "Soft Drop," JHEP **1405**, 146 (2014) doi:10.1007/JHEP05(2014)146 [arXiv:1402.2657 [hep-ph]].

[8] A. M. Sirunyan *et al.* [CMS Collaboration], "Particle-flow reconstruction and global event description with the CMS detector," JINST **12**, no. 10, P10003

(2017) doi:10.1088/1748-0221/12/10/P10003 [arXiv:1706.04965 [physics.ins-det]].

[9] L. Caminada, F. Canelli, S. Donato, D. Salerno and K. Schweiger, University of Zurich, "Fully hadronic $t\bar{t}H$ ($H \to b\bar{b}$) analysis using the Matrix Element Method". CMS AN-16-411.

[10] Cornelis, Tom. "Quark-gluon Jet Discrimination At CMS." arXiv preprint arXiv:1409.3072 (2014).

[11] CMS Collaboration, "Observation of a new boson at a mass of 125 GeV with the CMS experiment at the LHC", Phys. Lett. B 716 (2012) 30–61, *doi:10.1016/j.physletb.2012.08.021, arXiv:1207.7235*.

[12] ATLAS Collaboration, "Observation of a new particle in the search for the Standard Model Higgs boson with the ATLAS detector at the LHC", Phys. Lett. B 716 (2012) 1–29, *doi:10.1016/j.physletb.2012.08.020, arXiv:1207.7214*.

[13] The ATLAS and CMS Collaborations Collaboration, "Measurements of the Higgs boson production and decay rates and constraints on its couplings from a combined ATLAS and CMS analysis of the LHC pp collision data at $\sqrt{s} = 7$ and 8 TeV", Technical Report ATLAS-CONF-2015-044,CMS-PAS-HIG-15-002, CERN, Geneva, 2015.

[14] LHC Higgs Cross Section Working Group Collaboration, "Handbook of LHC Higgs Cross Sections: 4. Deciphering the Nature of the Higgs Sector", *arXiv:1610.07922*.

[15] C. Grojean, E. Salvioni, M. Schlaffer, and A. Weiler, "Very boosted Higgs in gluon fusion", JHEP 05 (2014) 022, doi:10.1007/JHEP05(2014)022, *arXiv:1312.3317*.

[16] "PARTON LUMINOSITY AND CROSS SECTION PLOTS", James Stirling, Imperial College London, "W.J. Stirling, private communication". `http://www.hep.ph.ic.ac.uk/~wstirlin/plots/plots.html`.

[17] "The Large Hadron Collider", CERN. `http://home.cern/topics/large-hadron-collider`

[18] Stephen Myers, "The large hadron collider 2008–2013," Int. J. Mod. Phys. A, 28 (2013) 1330035 [DOI: 10.1142/S0217751X13300354].

[19] C. Vernieri, "Search for resonances decaying to $H \to b\bar{b}$ pairs with the CMS experiment at the LHC," CERN-THESIS-2014-161, CMS-TS-2014-035.

[20] CMS Collaboration, "The CMS experiment at the CERN LHC," JINST 3 (2008) S08004. *doi:10.1088/1748-0221/3/08/S08004*

[21] "CMS Detector", CERN `https://cms.cern/detector`

[22] CMS Collaboration, "The CMS tracker system project: technical design report". Technical Design Report CMS. CERN, Geneva, 1998. CERN-LHCC-98-006, `https://cds.cern.ch/record/368412?ln=en`.

[23] CMS Collaboration, "The CMS tracker: addendum to the Technical Design Report". Technical Design Report CMS. CERN, Geneva, 2000. CERN-LHCC-2000-016, `https://cds.cern.ch/record/490194`.

[24] CMS Collaboration, "The CMS electromagnetic calorimeter project: technical design report". Technical Design Report CMS. CERN, Geneva, 1997. CERN-LHCC-97-033, `https://cds.cern.ch/record/349375`.

[25] CMS Collaboration, "Addendum to the CMS ECAL technical design report: changes to the CMS ECAL electronics". Technical Design Report CMS. CERN, Geneva, 2002. CERN-LHCC-2002-027, `http://cds.cern.ch/record/581342`.

[26] CMS Collaboration, "CMS: The hadron calorimeter technical design report". Technical Design Report CMS. CERN, Geneva, 1997. CERN-LHCC-97-31, `https://cds.cern.ch/record/357153?ln=en`.

[27] CMS Collaboration, "CMS: The muon project technical design report". Technical Design Report CMS. CERN, Geneva, 1997. CERN-LHCC-97-32, `https://cds.cern.ch/record/343814`.

[28] CMS Collaboration, "CMS, the magnet project: technical design report". Technical Design Report CMS. CERN, Geneva, 1997. CERN-LHCC-97-10, `https://cds.cern.ch/record/331056?ln=en`.

[29] "Particle flow in CMS", http://cerncourier.com/cws/article/cern/65034

[30] "The Higgs Boson", https://home.cern/topics/higgs-boson

[31] "The Higgs Mechanism", https://home.cern/topics/higgs-boson/origins-brout-englert-higgs-mechanism

[32] ATLAS Collaboration, "Measurements of Higgs boson production and couplings in diboson final states with the ATLAS detector at the LHC", Phys. Lett. B 726 (2013) 88, arXiv: 1307.1427 [hep-ex].

[33] CMS Collaboration, "Observation of a new boson with mass near 125 GeV in pp collisions at $\sqrt{s} = 7$ and 8 TeV", JHEP 06 (2013) 081, arXiv: 1303.4571 [hep-ex].

[34] "SM Higgs production cross sections at $\sqrt{s}$ = 13-14 TeV", https://twiki.cern.ch/twiki/bin/view/LHCPhysics/CERNYellowReportPageAt1314TeV2014